ment shown in Fig. 1. Because the change in volume fraction from $\phi_3$ to $\phi_2$ is quite subtle, the $LS_3$ structures are seen primarily in combination with the $LS_2$ and with defects in the transition region indicated in Fig. 4 [see Web figs. 1, 3, and 4 (19)]. At $\phi_1$ there are even fewer particles in the drying front, and filling the lowest points in a line parallel to the drying film results in the LS structure from Fig. 2. Our observations also explain the finding (21) that in holes in a polymer film in which three particles fitted, the drying front arranged the triangles with sides parallel to the drying front.

To create non–close-packed crystals of single-sized particles with our method, we first created a composite $LS_2$ binary crystal of alternating layers of inorganic (silica) and organic (polystyrene) particles. Then, the organic layer was removed by heating (rate 1°C/min) in an oven at 600°C for 4 hours in air. The resulting structure is a hexagonal non–close-packed (hncp) crystal (Fig. 5). This non–close-packed structure, with a low packing fraction of $\rho = 0.6046$ compared with the close-packed structure ($\rho = 0.7405$), is another example of how the layer-by-layer method can be used to create new crystal structures that cannot be grown in bulk.

We have demonstrated the formation of large areas of LS, $LS_2$, and $LS_3$ binary colloidal crystals using a nonequilibrium layer-by-layer growth process. We have explored only a small region of $\gamma$ values, and so there is a large scope for expanding on this work. The method is simple enough that it can be easily automated to create structures thicker than those shown here (22). By using surface templates (7), the method can be further extended by growing different crystal planes and new types of crystals with a well-defined crystal orientation (23). For example, using a square template will make it possible to grow CsCl-type binary structures. Our method may substantially expand the stoichiometries, compositions, and symmetries achievable with crystals of colloidal particles.
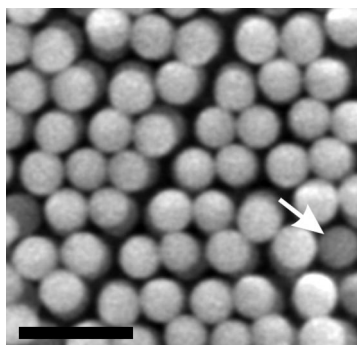


**Fig. 5.** SEM of the top layer of a hncp colloidal crystal. The arrow points to a particle from the bottom layer. Bar, 1 μm.

**References and Notes**

1. C. J. Kiely *et al.*, *Nature* **396**, 444 (1998).
2. M. J. Murray, J. V. Sanders, *Nature* **275**, 201 (1978).
3. _____, *Philos. Mag.* **43**, 721 (1980).
4. S. Hachisu, S. Yoshimura, *Nature* **283**, 188 (1980).
5. P. Bartlett, R. H. Ottewill, P. N. Pusey, *Phys. Rev. Lett.* **68**, 3801 (1992).
6. M. D. Eldridge, P. A. Madden, D. Frenkel, *Nature* **365**, 35 (1993).
7. A. van Blaaderen, R. Ruel, P. Wiltzius, *Nature* **385**, 321 (1997).
8. M. Heni, H. Lowen, *Phys. Rev. Lett.* **85**, 3668 (2000).
9. N. D. Denkov *et al.*, *Nature* **361**, 26 (1993).
10. P. Jiang, J. F. Bertone, K. S. Hwang, V. L. Colvin, *Chem. Mater.* **11**, 2132 (1999).
11. P. A. Kralchevsky, N. D. Denkov, *Curr. Opin. Colloid Interface Sci.* **6**, 383 (2001).
12. N. D. Denkov *et al.*, *Langmuir* **8**, 3183 (1992).
13. A. S. Dimitrov, K. Nagayama, *Langmuir* **12**, 1303 (1996).
14. Highly monodispersed silica particles (polydispersity < 3%) were prepared by microemulsion (24) followed by seeded growth.
15. K. P. Velikov, C. G. Christova, R. P. A. Dullens, A. van Blaaderen, data not shown.
16. J. V. Smith, *Geometrical and Structural Crystallography* (Wiley, New York, 1982).
17. A. R. Denton, N. W. Ashcroft, *Phys. Rev. A* **42**, 7312 (1990).
18. N. Hunt, R. Jardine, P. Bartlett, *Phys. Rev. E* **62**, 900 (2000).
19. Supplementary Web material is available on *Science* Online at www.sciencemag.org/cgi/content/full/296/5565/106/DC1.
20. R. Moessner, S. L. Sondhi, *Phys. Rev. B* **6322**, 224401 (2001).
21. Y. D. Yin, Y. N. Xia, *Adv. Mater.* **13**, 267 (2001).
22. Because the mechanism underlying the controlled drying technique is similar to that of industrial coating processes, in which good control over the thickness of the depositing layers and high automatization are achieved, we believe that scaling up of the process to an industrial scale is feasible.
23. A. van Blaaderen, P. Wiltzius, *Adv. Mater.* **9**, 833 (1997).
24. K. Osseoasare, F. J. Arriagada, *Colloid Surf.* **50**, 321 (1990).
25. We thank P. M. Chaikin, A. Moroz, A. Imhof, and M. Dogterom for helpful discussions. This work is part of the research program of the Stichting voor Fundamenteel Onderzoek der Materie (FOM), which is financially supported by the Nederlandse Organisatie voor Wetenschappelijk Onderzoek.

16 October 2001; accepted 5 March 2002

# Structure of Haloform Intercalated C₆₀ and Its Influence on Superconductive Properties

**Robert E. Dinnebier,¹ Olle Gunnarsson,¹ Holger Brumm,¹ Erik Koch,¹ Peter W. Stephens,² Ashfia Huq,² Martin Jansen¹\***

$CHCl_3$ and $CHBr_3$ intercalated $C_{60}$ have attracted particular interest after a superconductivity transition temperature ($T_c$) of up to 117 K was discovered. We have determined the structure using synchrotron x-ray powder-diffraction and found that the expansion of the lattice mainly takes place in one dimension (triclinic *b* axis), leaving planes of $C_{60}$ molecules on an approximately hexagonal, slightly expanded lattice. We have performed tight-binding band structure calculations for the surface layer. In spite of the slight expansion of the layers, for the range of dopings where a large $T_c$ has been observed, the density of states at the Fermi energy is smaller for $C_{60} \cdot 2CHCl_3$ and $C_{60} \cdot 2CHBr_3$ than for $C_{60}$. This suggests that the lattice expansion alone cannot explain the increase of $T_c$.

Using a field-effect transistor (FET), Schön *et al.* have demonstrated that chemical doping is not the only way to make the fullerenes metallic and superconducting. They showed that pristine $C_{60}$ can be field-doped and becomes superconducting with transition temperatures $T_c$ up to 11 K for electron doping (1) and 52 K for hole doping (2). For the chemically electron-doped fullerenes, $T_c$ increases with the lattice constant and is generally explained by the corresponding in-

crease in the density of states (DOS) (3–5). This trend was the motivation for investigating fullerene crystals intercalated with inert molecules that act as spacers to expand the lattice. And, indeed, it was found that $T_c$ increased to values of about 80 K for $C_{60} \cdot 2CHCl_3$ and 117 K for $C_{60} \cdot 2CHBr_3$, apparently confirming the assumption that in order to increase $T_c$ one simply has to increase the DOS (6).

We report structure determinations of the $C_{60} \cdot 2CHCl_3$ and $C_{60} \cdot 2CHBr_3$ cocrystals and give a comparison with pristine $C_{60}$, finding that intercalation of chloroform and bromoform does increase the volume per $C_{60}$ molecule. However, the increase is anisotropic and is mainly due to an expansion of the lattice perpendicular to the close-packed

¹Max-Planck-Institut für Festkörperforschung, Heisenbergstrasse 1, D-70569 Stuttgart, Germany. ²Department of Physics and Astronomy, State University of New York, Stony Brook, NY 11974, USA.

*To whom correspondence should be addressed. E-mail: m.jansen@fkf.mpg.de

planes, which are presumably the free surface on which the superconducting FETs have been grown. The in-plane expansion is only slight. In contrast to chemically electron-doped fullerenes, which are bulk superconductors, superconductivity in the field-doped materials is confined to the immediate neighborhood of the surface. The prepared surface is not necessarily a simple truncation of bulk; for example there may be reconstruction, different fullerene orientations, a different concentration of intercalants, etc. However, it is reasonable to expect that the lattice spacings of the three-dimensional (3D) structure should persist to the surface, and therefore estimates of the DOS derived from the 3D

structure will provide a useful insight into the superconductivity. Tight-binding calculations show that, in contrast to what one would expect based on the increase in $T_c$, the DOS for pristine $C_{60}$ is actually larger than for the cocrystals in the doping range where a large $T_c$ has been observed. Comparing $C_{60} \cdot 2CHCl_3$ and $C_{60} \cdot 2CHBr_3$, we find that although the DOS differs slightly, this is by far not enough to explain the difference in the observed transition temperatures.

$C_{60} \cdot 2CHCl_3$ and $C_{60} \cdot 2CHBr_3$ were obtained by dissolving $C_{60}$ in chloroform or bromoform, respectively, with further evaporation. High-resolution x-ray powder diffraction data of $C_{60} \cdot 2CHCl_3$ and $C_{60} \cdot 2CHBr_3$



**Fig. 1.** Scattered x-ray [$\lambda$ = 1.15015 ± 0.00002 Å] intensity for $C_{60} \cdot 2CHCl_3$ as a function of diffraction angle $2\Theta$ and temperature $T$. Scans were taken as the sample was being cooled; thereafter, each represents a range of about 10 K.
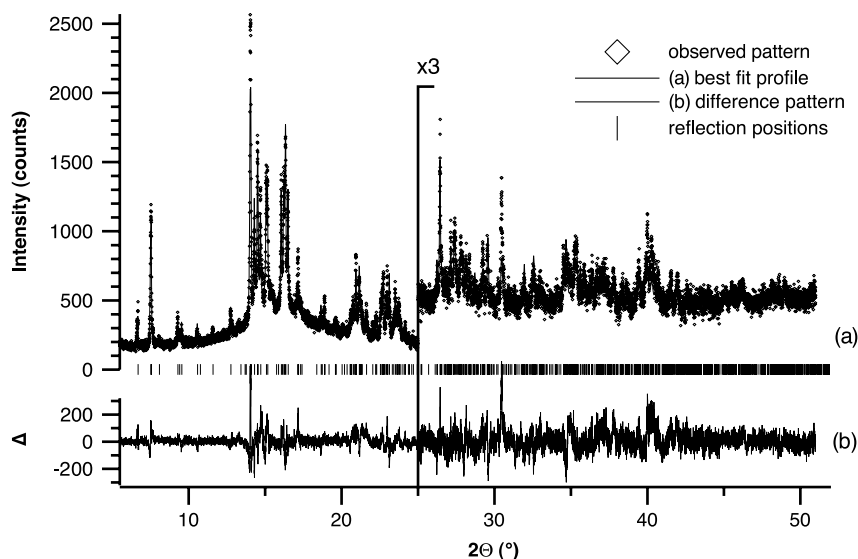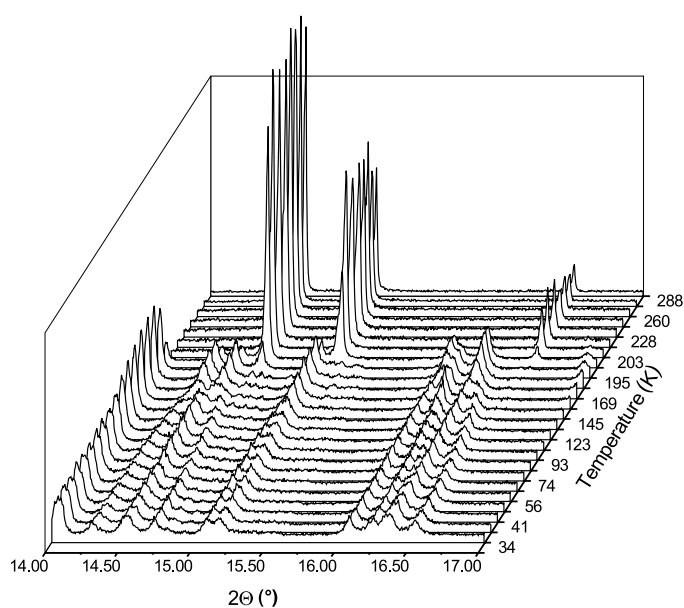


**Fig. 2.** Scattered x-ray intensity for $C_{60} \cdot 2CHCl_3$ at $T$ = 50 K as a function of diffraction angle $2\Theta$. The observed data (points) and the Rietveld fit (smooth curve) are shown at top (a), and the difference curve ($\Delta$) at bottom (b). Note vertical scale is magnified by 3, above 25°.

were collected at various temperatures (7) (Fig. 1). The crystal structures of the different phases of $C_{60} \cdot 2CHCl_3$ and $C_{60} \cdot 2CHBr_3$ were determined by Rietveld refinements (8) using flexible rigid bodies (9) (Fig. 2). Details of the experimental setup and the method of structure solution are given in Table 1 and (10).

At room temperature, $C_{60} \cdot 2CHCl_3$ and $C_{60} \cdot 2CHBr_3$ are isotypic to magnesium diboride (11) (space group P6/*mmm*, aluminum diboride structure type) in which a primitive hexagonal packing is formed by $C_{60}$ molecules with the trigonal prismatic voids at (1/3, 2/3, 1/2) and (2/3, 1/3, 1/2) fully occupied by chloroform or bromoform molecules, respectively. Therefore, the structure can be viewed as a sequence of alternating layers of $C_{60}$ and intercalated molecules perpendicular to the $c$ axis. With a sixfold axis through the center of the bucky ball (molecular symmetry $3\bar{m}$) and inversion centers in the center of the chloroform and bromoform molecules (molecular symmetry $3\bar{m}$), a minimum of twofold disorder is created, whereas Rietveld refinements confirm almost spherical shell electron density for the $C_{60}$ molecule and at least threefold disorder for the chloroform molecules (12–14).

Upon cooling, both materials pass through a monoclinic phase into a fully ordered low-temperature triclinic phase (space group $P\bar{1}$) at ~150 K with cell dimensions similar to those of the hexagonal room-temperature phase. The crystal structure of the triclinic low-temperature phase may be viewed as an anisotropically distorted hexagonal room-temperature structure. Whereas the dimensions of the hexagonal close-packed layers of $C_{60}$ molecules show only small distortions compared with the room-temperature structure, the distance between the $C_{60}$ layers (triclinic $b$ axis) increases considerably (Table 1), causing a decrease in dimensionality. The $C_{60}$ molecules are oriented such that two hexagons on opposite sides of the $C_{60}$ molecule are congruent with the triclinic $b$ axis (corresponding to the hexagonal $c$ axis) running through the centers of the hexagons and one of their three short carbon-carbon bonds oriented parallel to the $c$ axis (Fig. 3). This way, eight short bonds of a $C_{60}$ molecule (two each in the $\pm a$ and $\pm c$ directions) face short bonds of neighbor molecules with twisting angles between 60° and 90°. The differences in the orientation of the $C_{60}$ molecules between the low-temperature phases of $C_{60} \cdot 2CHCl_3$ and $C_{60} \cdot 2CHBr_3$ are only marginal. The shortest carbon-carbon distances (Table 2) occur between the $C_{60}$ molecules within a layer along the $a$ and $c$ axis (~3.3 Å). In contrast, the shortest carbon-carbon distances between $C_{60}$ molecules of consecutive layers increases considerably when going from chloroform-doped (~3.6 Å) to bro-

moform-doped ($\sim$3.8 Å) $C_{60}$, which is in accordance with the observed increase in the lattice parameters. The orientation of the chloroform and bromoform molecules in the two trigonal prismatic voids are related by inversion symmetry. Two halogen atoms point toward the middle between two $C_{60}$ molecules of consecutive layers, whereas the third halogen atom points either up or down. Consecutive voids along the $b$ axis show the same orientation. The decrease of disorder from the hexagonal to the triclinic structures is accompanied by a decrease of the average crystalline coherence length (domain size) from $\sim$7 $\mu$m to 0.2 $\mu$m (in case of $C_{60}{\cdot}2CHCl_3$), causing severe peak broadening. It should be noted that despite the low quality of the powder patterns at low temperature, the weighted profile R-value (R-wp) of the triclinic low-temperature phase is sensitive enough to determine the orientation of the $C_{60}$ molecule within reasonable accuracy. The R-wp of a completely misaligned $C_{60}$ molecule deviates by more than 3%. Heating-cooling cycles showed pronounced hystereses (up to 40 K) and coexistence of the different phases over a large temperature range. In general, the transition temperature and the existence of the different phases of $C_{60}{\cdot}2CHCl_3$ and $C_{60}{\cdot}2CHBr_3$ depends strongly on their thermal history. In the case of $C_{60}{\cdot}2CHCl_3$, additional intermediate phases of low symmetry occurred during slow cooling. At the low temperatures where superconductivity is observed, essentially all the material is transformed into the thermodynamically stable low-temperature phase, as described above.

In the $C_{60}$ compounds, the electron-phonon coupling $\lambda$ is described as a product of an intramolecular coupling and the electron DOS. Because the intramolecular coupling should be essentially the same for all $C_{60}$ compounds, the focus has been on the DOS, because an increase in the DOS should increase $\lambda$ and $T_c$. This approach was successfully used to interpret the results for $A_3C_{60}$ (A = K, Rb) (4) and was the motivation behind the work of Schön et al. (6). Here, we compare the different intercalated $C_{60}$ compounds at fixed doping, as in $A_3C_{60}$. The main change is then expected to be the increase in the DOS as the lattice is expanded (6).

To describe the electronic structure of $C_{60}{\cdot}2CHCl_3$ and $C_{60}{\cdot}2CHBr_3$ we use a tight-binding formalism (15, 16) that describes the variation of $T_c$ for $A_3C_{60}$ (A = K, Rb) (17). We put one radial 2p orbital on each carbon atom and calculate the molecular orbitals (MO) of a free $C_{60}$ molecule. Only the five-fold degenerate $h_u$ MO is kept, and the hopping integrals between the $h_u$ MOs on different molecules are calculated. The resulting Hamiltonian matrix is diagonalized. The cou-

pling to the $CHCl_3$ or $CHBr_3$ molecules is neglected, because their levels are energetically well separated from the $C_{60}$ $h_u$ (18) orbital. Because the strong electric field should confine the charge carriers to the surface layer (2, 19), we consider the close-packed (010) and (111) surfaces of the $P\bar{1}$ and $Pa\bar{3}$ (20) structures, respectively.

Fig. 4 shows the calculated densities of states. We focus on the doping range where substantial $T_c$'s have been observed ( p = 2 to 3.5). We find that the DOS for $C_{60}$ exceeds that of $C_{60}{\cdot}2CHCl_3$, contrary to what was expected from the observed $T_c$'s. This might seem surprising, given that the surface area per molecule for $C_{60}{\cdot}2CHCl_3$ (86.5 Å$^2$) is larger than for $C_{60}$ (85.4 Å$^2$). The reason is that the hopping mainly takes place via a few
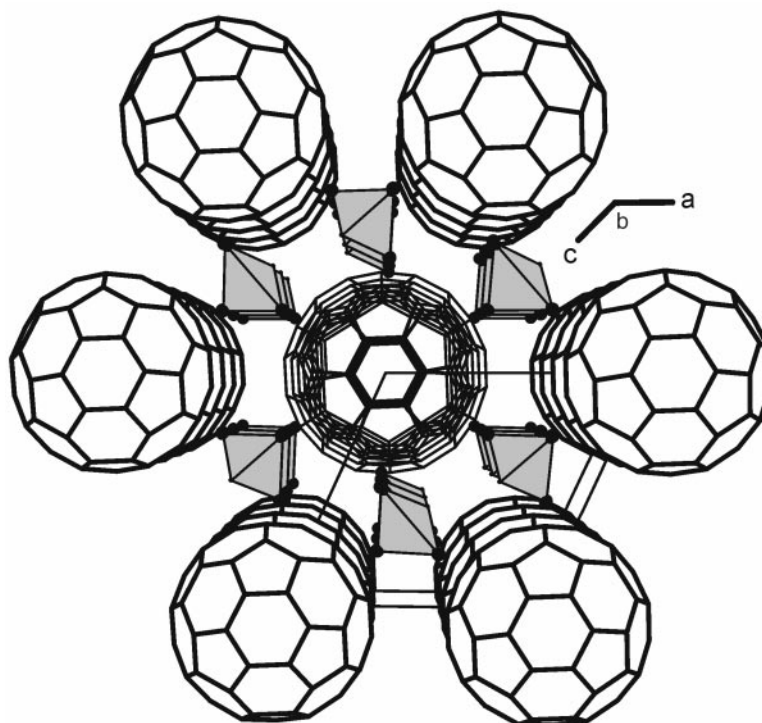


**Fig. 3.** Crystal structure of the low-temperature phase of $C_{60}{\cdot}2CHCl_3$ at $T$ = 50 K (isotypic to $C_{60}{\cdot}2CHBr_3$) in a view along $b$ axis showing the close relation to the hexagonal room-temperature phase.

**Table 1.** Crystallographic data for the low-temperature phase of $C_{60}{\cdot}2CHCl_3$ and $C_{60}{\cdot}2CHBr_3$. R-p, R-wp, and R-F$^2$ refer to the Rietveld criteria of fit for profile and weighted profile, respectively, defined in (29). Numbers in parentheses are errors in the last significant digit; for comparison, the lattice parameter of pristine $C_{60}$ at $T$ = 5 K is 9.9284(1) $\cdot \sqrt{2}$ Å in $Pa\bar{3}$ (28).

|  | $C_{60}{\cdot}2CHCl_3$ | $C_{60}{\cdot}2CHBr_3$ |
|---|---|---|
| Temperature (K) | 50 | 80 |
| Formula weight (g/mol) | 959.42 | 1226.15 |
| Space group | $P\bar{1}$ | $P\bar{1}$ |
| Z | 1 | 1 |
| $a$ (Å) | 9.8361(3) | 9.8982(3) |
| $b$ (Å) | 10.0906(3) | 10.3386(3) |
| $c$ (Å) | 9.8179(3) | 9.8993(3) |
| $\alpha$ (°) | 101.363(2) | 100.951(2) |
| $\beta$ (°) | 116.457(2) | 115.920(2) |
| $\gamma$ (°) | 79.783(2) | 78.202(3) |
| $V$ (Å$^3$) | 850.82(5) | 886.04(5) |
| $\rho$-calc (g/cm$^3$) | 1.872 | 2.298 |
| 2$\Theta$ range (°) | 5 to 49.76 | 3 to 44.0 |
| Step size (°2$\Theta$) | 0.005 | 0.003 |
| Wavelength (Å) | 1.15015(2) | 1.15052(2) |
| $\mu$ (1/cm) (100% packing) | 20.8 | 35.4 |
| R-p (%) | 7.9 | 9.0 |
| R-wp (%) | 10.0 | 11.7 |
| R-F$^2$ (%) | 21.6 | 16.3 |
| Number of reflections | 756 | 607 |

**Fig. 4.** DOS for the (010) surface of $C_{60}\cdot 2CHCl_3$, $C_{60}\cdot 2CHBr_3$ and the (111) surface of pure $C_{60}$. (**A**) DOS as a function of energy $\varepsilon$. We have introduced a Lorentzian broadening (full width at half maximum) of 0.02 eV. (**B**) DOS as a function of the hole doping p. For p from 2 to 3.5, a substantial $T_c$ is observed.
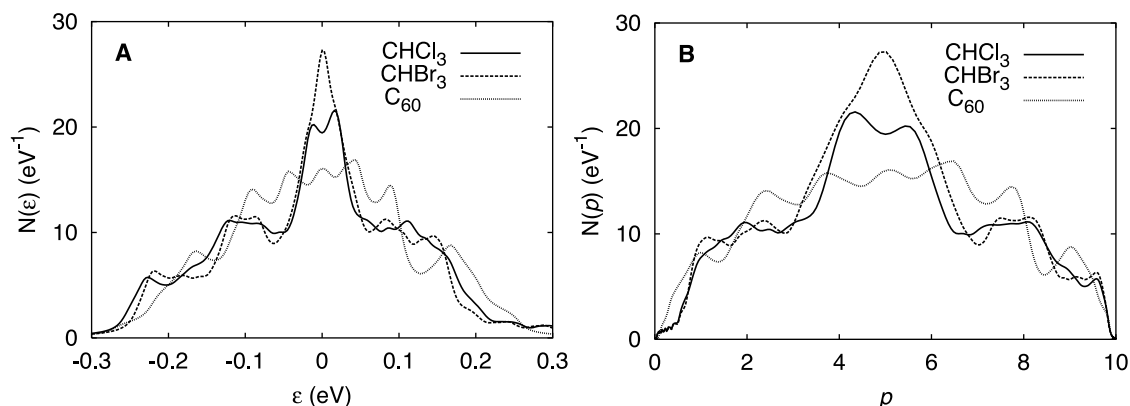


**Table 2.** Selected bond lengths and torsion angles for the low-temperature phases of $C_{60}\cdot 2CHCl_3$ at $T = 50$ K and of $C_{60}\cdot 2CHBr_3$ at $T = 80$ K. Realistic standard deviations have been obtained by multiplication of the Rietveld estimates by a factor of 6 in accordance with (30) and are on the order of 0.01 Å for distances and 2° for the torsion angles. For comparison, the distance between the $C_{60}$ molecules in pristine $C_{60}$ at $T = 5$ K is 9.9284(1) Å in $Pa\bar{3}$ [$a = 9.9284(1)\cdot\sqrt{2}$ Å] (28).

|  | $C_{60}\cdot 2CHCl_3$ | $C_{60}\cdot 2CHBr_3$ |
|---|---|---|
| **Distances (Å)** | | |
| C–C ($C_{60}$) intramolecular | 1.45 | 1.46 |
| C=C ($C_{60}$) intramolecular | 1.39 | 1.40 |
| C–C ($C_{60}$) intermolecular (along $a$, $c$) | 3.26, 3.28 | 3.28, 3.30 |
| C–C ($C_{60}$) intermolecular (along $a+c$) | 3.42 | 3.51 |
| C–C ($C_{60}$) intermolecular (along $b$) | 3.63 | 3.81 |
| $C_{60}$-$C_{60}$ | 9.8361(3) | 9.8982(3) |
| C–Cl/Br intramolecular | 1.78 | 1.97 |
| C–H intramolecular | 1.05 (fixed) | 1.05 (fixed) |
| C–H intermolecular | 2.67 | 2.78 |
| C–Cl/Br intermolecular | 3.33 | 3.33 |
| **Torsion angles (°)** | | |
| C=C ($C_{60}$) intramolecular | 76. 93 | 58. 59 |

"contact atoms." Thus, the hopping depends on the relative phases of the $h_u$ orbitals at these atoms. These phases are relatively unfavorable for the $Pa\bar{3}$ structure of pure $C_{60}$ compared with the $P\bar{1}$ structure of $C_{60}\cdot 2CHCl_3$, making the hopping somewhat weaker for $C_{60}$.

In $C_{60}\cdot 2CHCl_3$ and $C_{60}\cdot 2CHBr_3$ the relative orientations of the molecules are similar. The lattice expansion leads to an overall larger DOS, but over most of the doping range of 2 to 3.5 the DOS is increased by at most 10%. Solving the isotropic Eliashberg equations using realistic parameters (21) we find, however, that the DOS of $C_{60}\cdot 2CHBr_3$ would have to be about 25 to 35% larger than for $C_{60}\cdot 2CHCl_3$ in order to explain the change in $T_c$. Also for electron doping the difference in $T_c$ between $C_{60}\cdot 2CHCl_3$ and $C_{60}\cdot 2CHBr_3$ cannot be explained based on the DOS. The above conclusions persist when the DOS is broadened by 0.2 eV, simulating the effect of the large phonon energy.

What, then, might cause the observed strong enhancement of $T_c$? What comes to mind first is that superconductivity may not be limited to the surface layer. However, to obtain a substantial doping, the levels in the surface layer have to be well separated from those in layers underneath

(19). Therefore their contribution to the DOS can be expected to be small. Also the strong electric field in the surface layer may play an important role. Our estimates suggest, however, that its effect on the DOS would not change the conclusions (22). There could also be some coupling to the vibrational modes of $CHCl_3$ and $CHBr$, which might tend to enhance $T_c$ (23). As discussed above, the DOS is quite sensitive to the orientations of the $C_{60}$ molecules, which could be different at the surface. For instance, the $CHCl_3$ and $CHBr_3$ molecules because of their dipole moment would tend to align with the electric field at the surface, possibly influencing the orientations of the molecules. The surface of pristine $C_{60}$ could also be reconstructed in such a way that its DOS is reduced.

Here we have based our discussion on the DOS at the Fermi energy. This is the accepted approach for describing the variation of $T_c$ for $A_3C_{60}$ (4), i.e., as a function of the lattice parameter for fixed doping. However, it does not describe the strong doping dependence of $T_c$ (24), as the DOS of the merohedrally disordered $A_3C_{60}$ is rather constant (25). In addition, for the electron-doped systems, field doping and chemical doping give similar values of $T_c$ (1, 6). This is surprising, because the reduced number of neighbors at

the surface should lead to a larger DOS and a correspondingly higher $T_c$. These problems raise questions about the conventional interpretation in terms of the DOS.

**References and Notes**

1. J. H. Schön, C. Kloc, R. C. Haddon, B. Batlogg, *Science* **288**, 656 (2000).
2. J. H. Schön, C. Kloc, B. Batlogg, *Nature* **408**, 549 (2000).
3. M. J. Rosseinsky *et al.*, *Phys. Rev. Lett.* **66**, 2830 (1991).
4. R. M. Fleming *et al.*, *Nature* **352**, 787 (1991).
5. O. Gunnarsson, *Rev. Mod. Phys.* **69**, 575 (1997).
6. J. H. Schön, C. Kloc, B. Batlogg, *Science* **293**, 2432 (2001).
7. X-ray powder diffraction data of $C_{60}\cdot 2CHCl_3$ and $C_{60}\cdot 2CHBr_3$ were collected at various temperatures in a closed-cycle helium cryostat on beamline X3B1 of the Brookhaven National Synchrotron Light Source in transmission geometry with the samples sealed in 0.7-mm lithium borate glass (No. 50) capillaries.
8. H. M. Rietveld, *J. Appl. Crystallogr.* **2**, 65 (1969).
9. R. E. Dinnebier, *Powder Diffr.* **14**, 84 (1999).
10. Supplementary figures and details of experimental procedures are available on *Science* Online at www.sciencemag.org/cgi/content/full/296/5565/109/DC1.
11. M. E. Jones, R. E. Marsh, *J. Am. Chem. Soc.* **76**, 1434 (1954).
12. M. Jansen, G. Waidmann, *Z. Anorg. Allg. Chem.* **621**, 14 (1995).
13. G. Waidmann, thesis, University of Bonn (1996).
14. L. A. Solovyov, N. V. Bulina, G. N. Churilov, *Russ. Chem. Bull.* **50**, 78 (2001).
15. O. Gunnarsson, S. Satpathy, O. Jepsen, O. K. Andersen, *Phys. Rev. Lett.* **67**, 3002 (1991).
16. N. Laouini, O. K. Andersen, O. Gunnarsson, *Phys. Rev. B* **51**, 17446 (1995).
17. The intermolecular parameters are $v_\sigma = 0.296d$ $\exp[-(d - 3.1)/L]$ eV, $v_\pi = -v_\sigma/4$ and $L = 0.91$ Å, where $d$ is the atomic separation. $L$ was adjusted to obtain a variation of $N(0)$ (26, 27) needed to describe the $T_c$ of $A_3C_{60}$ (A = K, Rb). The intramolecular hopping integrals are −3.17 and −3.40 eV for the single and double bonds, respectively.
18. Density functional calculations put the highest occupied and lowest unoccupied MOs of a free $CHCl_3$ molecule 1.7 eV below and 3.5 eV above the $h_u$ orbital of the free $C_{60}$ molecule, respectively. The corresponding numbers for $CHBr_3$ are 1.1 and 2.7 eV.
19. S. Wehrli, D. Poiblac, T. M. Rice, *Eur. Phys. J. B* **23**, 345 (2001).
20. To make the calculations for the $P\bar{1}$ and the $Pa\bar{3}$ structures as comparable as possible, the $C_{60}$ coordinates determined for $C_{60}\cdot 2CHCl_3$ were used also for the $Pa\bar{3}$ structure, instead of the slightly different coordinates found by David *et al.* (28).
21. Guided by estimates from photoemission (26), we have, e.g., used a single Einstein phonon with the energy 1000 K, the Coulomb pseudopotential $\mu = 0.4$ and the band width 0.5 eV, as well as variations around this parameter set.

22. Applying an electric field of 0.2 V/Å in a nonself consistent calculation left the relative magnitudes of the DOS for $C_{60}$ and $C_{60} \cdot 2CHCl_3$ largely uncharged in the doping range from 2 to 3.5.
23. A. K. Bill, V. Z. Kresin, unpublished data.
24. T. Yildirim et al., Phys. Rev. Lett. **77**, 167 (1996).
25. M. P. Gelfand, J. P. Lu, Phys. Rev. Lett. **68**, 1050 (1992).
26. O. Gunnarsson et al., Phys. Rev. Lett. **74**, 1875 (1995).
27. M. Schluter, M. Lannoo, M. Needels, G. A. Baraff, D. Tomanek, J. Phys. Chem. Solids **53**, 1473 (1992).
28. W. I. F. David et al., Nature **353**, 147 (1991).
29. J. I. Langford, D. Louer, Rep. Prog. Phys. **59**, 131 (1996).
30. R. J. Hill, L. M. D. Cranswick, J. Appl. Crystallogr. **27**, 802 (1994).
31. O.G. thanks the Max-Planck-Forschungspreis, and R. D. thanks the Fonds der Chemische Industrie (FCI)

# A High-Resolution Paleoclimate Record Spanning the Past 25,000 Years in Southern East Africa

**Thomas C. Johnson,[1]\* Erik T. Brown,[1] James McManus,[1] Sylvia Barry,[1]† Philip Barker,[2] Françoise Gasse[3]**

High-resolution profiles of the mass accumulation rate of biogenic silica and other geochemical proxies in two piston cores from northern Lake Malawi provide a climate signal for this part of tropical Africa spanning the past 25,000 years. The biogenic silica mass accumulation rate was low during the relatively dry late Pleistocene, when the river flux of silica to the lake was suppressed. Millennial-scale fluctuations, due to upwelling intensity, in the late Pleistocene climate of the Lake Malawi basin appear to have been closely linked to the Northern Hemisphere climate until 11 thousand years ago. Relatively cold conditions in the Northern Hemisphere coincided with more frequent north winds over the Malawi basin, perhaps resulting from a more southward migration of the Intertropical Convergence Zone.

Tropical Africa was cooler and drier during the last glacial maximum than it is today (1, 2). However, we have little information about higher frequency climate variability in the African tropics during the last glacial period or about the transition from ice age to interglacial conditions. Was there an abrupt shift to warm and wetter conditions? Was there monotonic evolution, or change by fits and starts? How does climate change in the African tropics relate to the signals registered in the ice sheets of Greenland and Antarctica? Some answers have been forthcoming from studies of lake sediments throughout much of Africa (1). But knowledge of the timing and nature of climate variability in much of tropical Africa still eludes us, as does an understanding of its role in the global climate system.

Here, we present a high-resolution record of climate dynamics from two piston cores spanning the past 25,000 years in northern Lake Malawi (Fig. 1). We recovered six piston cores and seven multicores from the north basin of Lake Malawi in 1998 as part of an expedition of the International Decade for the East African Lakes (IDEAL) (3).

Two of the cores were selected for more detailed study: M98-1P (at 10°15.9′S, 34°19.1′E, and a 403-m depth) and M98-2P (at 9°58.6′S, 34°13.8′E, and a 363-m depth) (Fig. 1). Radiocarbon dates were obtained on organic matter at six horizons in M98-1P and at eight horizons in M98-2P, using accelera-

tor mass spectrometry (Table 1). Both cores show a distinct shift in sedimentation rates from about 0.2 mm per year before 12 thousand years ago (ka) to about 0.5 mm per year after that time. We sampled these cores at 1-cm intervals for biogenic silica analysis and at a lower resolution for other parameters, including incompatible trace metals, total and inorganic phosphorus, diatom concentration, and species assemblages.

The percent biogenic silica in the cores reflects the abundance of diatoms in the lake sediments. Other sources of biogenic silica (e.g., phytoliths and sponge spicules) are rare in comparison to diatoms. Diatoms dominate the phytoplankton in Lake Malawi throughout most of the year, especially during the dry windy season in austral winter, when primary production in the lake is at a maximum (4, 5). The percent biogenic silica was converted to a mass accumulation rate (BSi MAR) based on sediment porosity and density and the linear sedimentation rates.

The BSi MAR profiles of the two cores correlate well, and, at the millennial scale, show similarities to the Greenland ice core record (GRIP) of the oxygen isotope ratio ($\delta^{18}O$) (Fig. 2). Both BSi MAR profiles show lower mean values in the Pleistocene sediments than in the Holocene deposits, and the transition from Pleistocene to Holocene values occurs in two abrupt steps, with an intervening interval of Pleistocene-like conditions. The timing of the glacial to interglacial transition, however, is different from the timing recorded in the GRIP record. The profiles exhibit an abrupt shift to higher values, beginning at about 13 ka, and then show a return to lower values about a thousand years later. The BSi MAR rises abruptly once again around 10.3 ka, to Holocene values. The initial rise to Holocene-like values at 13 ka
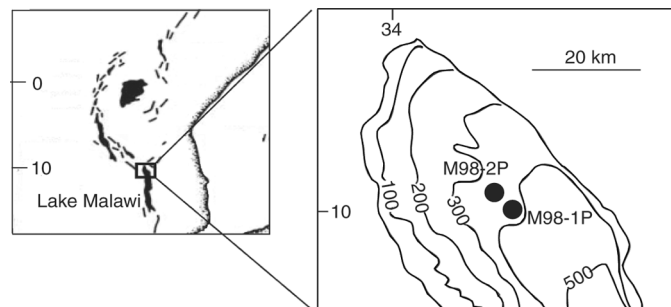
[1]Large Lakes Observatory, University of Minnesota Duluth, Duluth, MN 55812, USA. [2]Department of Geography, Lancaster University, Lancaster LA1 4YB, UK. [3]Centre Européen de Recherche et d'Enseignement en Géosciences de l'Environnement, Centre National de la Recherche Scientifique, Université d'Aix-Marseille III, BP 80, 13545 Aix-en-Provence, Cedex 04, France.

\*To whom correspondence should be addressed. E-mail: tcj@d.umn.edu
†Present address: Harvard Forest, Post Office Box 68, Petersham, MA 01366, USA.

**Fig.1.** Bathymetry of the north basin of Lake Malawi, showing the locations of the core sites. The contours are in meters.